The Planetary Science Journal, 4:134 (12pp), 2023 July https://doi.org/10.3847/PSJ/acde7f

On Ganymede's Magnetic Quadrupolar Strength

A. M. Plattner[1], C. L. Johnson[2,3], M. J. Styczinski[4,6], S. D. Vance[4], and A. C. Mills[5]
[1] Department of Geological Sciences, University of Alabama, Tuscaloosa, AL 35487, USA; amplattner@ua.edu
[2] Department of Earth, Ocean and Atmospheric Sciences, University of British Columbia, Vancouver, BC V6T 1Z4, Canada
[3] Planetary Science Institute, Tucson, AZ 85719, USA
[4] Jet Propulsion Laboratory, California Institute of Technology, Pasadena, CA 91109, USA
[5] Department of Geosciences, Baylor University, Waco, TX 76798, USA
Received 2023 March 30; revised 2023 June 5; accepted 2023 June 13; published 2023 July 31

Abstract

Ganymede is the only moon in our solar system known to have a large-scale intrinsic magnetic field, likely generated in the moon's metallic core. Initial analyses of Galileo spacecraft measurements concluded that Ganymede's intrinsic magnetic field is dominated by a magnetic dipole and that quadrupolar contributions are exceptionally weak. These findings have influenced the development of models for Ganymede's core dynamo over the past two decades, some concluding that Ganymede's dynamo is limited to the innermost part of Ganymede's core. Here, we reassess Ganymede's internal field contributions based on the magnetic measurements from close Galileo flybys of Ganymede (G1, G2, G7, G8, G28, and G29), adding the recent Juno flyby. We find that presently available data cannot constrain Ganymede's quadrupole moment, as we demonstrate by constructing models with a range of quadrupole moments, including relative values comparable to those at the Earth. As a consequence, global analysis of available data cannot constrain the spatial limits of Ganymede's core dynamo. Incorporating ocean induction for a range of Ganymede ocean models indicates that ocean induction may be present, but that available magnetic data cannot discern between end-member cases for Ganymede ocean models.

Unified Astronomy Thesaurus concepts: Ganymede (2188); Magnetic fields (994); Planetary cores (1247)

1. Introduction

Ganymede's intrinsic magnetic field, identified by measurements from the Galileo spacecraft (Kivelson et al. 1996), makes it the only moon in the solar system with a magnetic field that is sufficiently strong to create a global magnetosphere. Schubert et al. (1996) and Sarson et al. (1997) argued that Ganymede's magnetic field is generated by a dynamo inside Ganymede's core.

Kivelson et al. (2002) derived two spherical harmonic models for Ganymede's internal magnetic field. The first described Ganymede's internal magnetic field as a superposition of an internal dipolar and quadrupolar field (spherical harmonic degrees 1 and 2; see Section 2). The second replaced the quadrupolar field with an induced dipolar field inferred to result from electric currents induced in Ganymede's putative, electrically conductive ocean by oscillations in the magnetic field applied by Jupiter. Because both representations fit the data similarly, but the model with the induced field used fewer parameters, Kivelson et al. (2002) preferred the induced model over the quadrupolar model. A spherical harmonic model of Weber et al. (2022), which included new flyby measurements by Juno, found a similarly weak quadrupolar contribution. Their quadrupolar model provided a minimally improved fit to the data compared to a purely dipolar model. Thus, Weber et al. (2022) also favored their purely dipolar model over their dipolar plus quadrupolar model.

Saur et al. (2015) provided independent support for an induced magnetic field from Ganymede's ocean. They found that induction within the ocean decreased the predicted rocking of Ganymede's auroral ovals from about 5°, to closer to the observed 2°. Saur et al. (2015) determined that the observed reduction in rocking is consistent with an ocean with electrical conductivity of at least 0.09 S m^{-1} that extends to relatively close to the surface (<30 km thick ice shell). They concluded that the presence of an induced field implies that the quadrupole moment determined by Kivelson et al. (2002) gives an upper bound on Ganymede's true quadrupolar field strength.

Some, but not all, thermal evolution and dynamo models for Ganymede's magnetic field (e.g., Hauck et al. 2006; Bland et al. 2008; Zhan & Schubert 2012; Christensen 2015a, 2015b; Rückriemen et al. 2015) have been influenced by these results. One interpretation of the small quadrupole-to-dipole ratio is that Ganymede's dynamo source radius is only 130 km (about $0.05r_G$; Kivelson et al. 2002). This would limit the core dynamo to the innermost part of Ganymede's core, which is estimated to have a radius of between 650 and 900 km (about $0.25r_G$ to $0.34r_G$; Schubert et al. 2004). Kivelson et al. (2002) cautioned against overinterpreting their source radius results. Such a reported source radius is likely unreliable because dipole and quadrupole terms of core magnetic fields tend to not fit the trend observed in higher-degree powers. Estimations of source radii from degree powers are typically done using harmonics of degree 3 and greater (Lowes 1974).

The goal of this work is to assess whether presently available magnetic field data can constrain the quadrupolar component of Ganymede's magnetic field and whether it is indeed exceptionally weak compared with the magnetic fields of other planetary bodies in our solar system, with the exception of Saturn (Christensen 2015a). A finding that this may not be the

[6] NASA Postdoctoral Program Fellow.

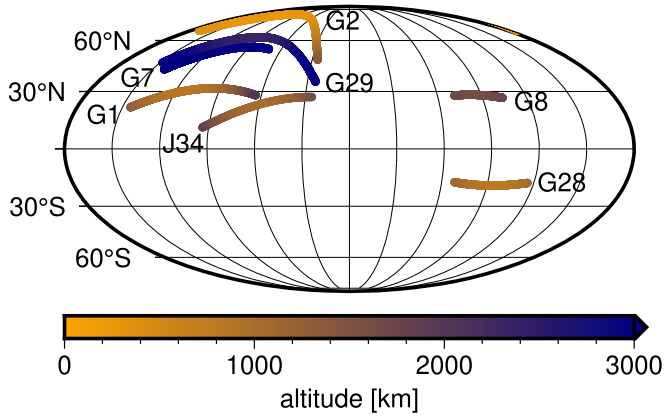

Figure 1. Spacecraft tracks for Galileo (G1–G29) and Juno (J34) for the time ranges in Table 1. A Mollweide projection is used for Ganymede's IAU coordinate system. The map is centered on Ganymede's sub-Jovian point, with Ganymede's leading hemisphere on the left.

case would have a substantial impact on dynamo models for Ganymede.

We construct a range of models from Galileo and Juno data using the approach described in Section 2 to examine the uncertainty in the relative powers of the dipolar and quadrupolar components of Ganymede's core magnetic field (Section 3). In Section 4, we discuss the consequences of these uncertainties on constraining dynamo models. We use Galileo flybys G1, G2, G7, G8, G28, and G29, as well as Juno flyby J34 (Figure 1). We do not use Galileo flybys G9 and G12, because they were too far from Ganymede to provide a suitable sampling of the intrinsic field. Here, we use the term "internal magnetic field" for any magnetic field with sources inside the planetary body. Internal magnetic fields thus include core dynamo magnetic fields ("intrinsic fields") as well as magnetic fields induced inside a planetary body by time-varying external fields. We assess whether induced magnetic fields affect our results by modeling and subtracting such fields for a range of Ganymede internal structures (Section 2.2).

2. Methods

To calculate the intrinsic contributions of Ganymede's magnetic field, we adopt an approach analogous to that of Kivelson et al. (2002). We represent the magnetic field within Ganymede's magnetopause as a superposition of three contributions: Ganymede's internal field $\boldsymbol{B}^{\rm int}$ (including intrinsic and induced fields), Jupiter's magnetospheric field $\boldsymbol{B}^{J}$, and a time-varying external field $\boldsymbol{B}^{U}$ capturing fields arising, for example, from Ganymede magnetopause currents:

$$\boldsymbol{B} = \boldsymbol{B}^{\rm int} + \boldsymbol{B}^{J} + \boldsymbol{B}^{U}. \tag{1}$$

In Section 2.1, we discuss the spherical harmonic model of Ganymede's internal magnetic field $\boldsymbol{B}^{\rm int}$ and our modeling of $\boldsymbol{B}^{J}$ and $\boldsymbol{B}^{U}$. Interpretations of Ganymede's dynamo are drawn from the results for $\boldsymbol{B}^{\rm int}$, as described in Section 4. In a first step (Section 2.1), we assume that our internal magnetic field is dominated by a core dynamo (intrinsic) field that is static over the time period of the observations. In Section 2.2, our internal magnetic field model $\boldsymbol{B}^{\rm int}$ additionally contains a time-dependent field $\boldsymbol{B}^{\rm ind}$—the expected induced magnetic field arising from induction in Ganymede's ocean.

2.1. Spherical Harmonic Models of Ganymede's Magnetospheric Field

Planetary magnetic fields $\boldsymbol{B}^{\rm int}$ originating from inside a planetary body can be described as the spatial derivative of a scalar magnetic potential V:

$$V(r, \theta, \phi) = r_p \sum_{l=1}^{L_{\rm max}} \sum_{m=0}^{l} \left(\frac{r_p}{r}\right)^{l+1} \times (g_l^m \cos m\phi + h_l^m \sin m\phi) P_l^m(\cos\theta), \tag{2}$$

$$\boldsymbol{B}^{\rm int} = -\boldsymbol{\nabla} V, \tag{3}$$

if no external magnetic fields and no magnetic sources are present in the region of representation. In Equation (2), the variables r, θ, and ϕ are the radius, colatitude, and east longitude, P_l^m are the Schmidt semi-normalized associated Legendre functions for spherical harmonic degree l and order m (e.g., Blakely 1995; Winch et al. 2005), and r_p is the planetary body's radius; for Ganymede, $r_p = r_G = 2631.2$ km. The smallest spatial scale described by such a representation is given by the maximum spherical harmonic degree $L_{\rm max}$, which also determines the number of model parameters—the Gauss coefficients g_l^m and h_l^m for $\boldsymbol{B}^{\rm int}$. The power per spatial length scale of the magnetic field evaluated at the surface of the planetary body is represented by the Mauersberger–Lowes spherical harmonic power spectrum:

$$R(l) = (l+1) \sum_{m=0}^{l} (g_l^m)^2 + (h_l^m)^2. \tag{4}$$

In all of our analysis, we use IAU coordinates for Ganymede. In their analysis, Kivelson et al. (2002) used Ganymede-centric G-Phi-Omega (GPhiO) coordinates, in which the x-axis is aligned with the direction of corotational flow, the z-axis is parallel to the Jovian spin axis, and the y-axis completes the right-handed set (roughly toward Jupiter's center). Because Ganymede's orbit has nonzero inclination and eccentricity, the GPhiO coordinate system varies over time with respect to a Ganymede-fixed coordinate system. Ganymede's IAU coordinates have the x-axis directed roughly toward Jupiter's center (oriented from Ganymede's center to a specific surface feature on Ganymede), the z-axis parallel to Ganymede's spin axis, and the y-axis completing the right-handed set (roughly opposite the orbital velocity). The spherical version of the IAU coordinates is referred to in Galileo data as GSPRH. The GPhiO x–y plane is approximately a 90° rotation about the IAU z-axis of the IAU x–y plane, and the z-axes are nearly aligned, with these differences varying throughout Ganymede's orbit. Because IAU coordinates are fixed to the body, they are the most natural choice for representing Ganymede's core dynamo (intrinsic) field, as intrinsic magnetic moments are generally assumed to be fixed to the orientation of the metallic core, and we thus use the GSPRH system here. We note that external currents align with the GPhiO coordinate system, which may thus be better suited to express external fields. The practical differences between the IAU and GPhiO coordinate system is small and thus only minimally affects the outcome of our analysis.

Before solving for a representation of Ganymede's internal magnetic field $\boldsymbol{B}^{\rm int}$ and the time-varying external magnetic field $\boldsymbol{B}^{U}$ within Ganymede's magnetopause, we subtract Jupiter's magnetic field $\boldsymbol{B}^{J}$ from the data. In this work, we model each

Table 1
Time Ranges and Jupiter's Magnetic Field for Each Flyby of Galileo and Juno

Flyby	Date	Start	Finish	B_x^J mn (slp)	B_y^J mn (slp)	B_z^J mn (slp)
G1	1996 Jun 27	06:24:56	06:35:58	–78 (–0.2)	18 (1.5)	–71 (0.5)
G2	1996 Sep 6	18:57:38	19:05:27	–69 (–0.4)	–11 (0.4)	–89 (0.0)
G7	1997 Apr 5	07:07:53	07:17:52	73 (0.0)	–0.5 (–0.2)	–79 (0.0)
G8	1997 May 5	15:53:42	15:57:51	–7 (1.0)	10 (0.0)	–86 (0.0)
G28	2000 May 20	10:08:05	10:12:19	78 (0.4)	3.5 (–0.3)	–75 (–0.1)
G29	2000 Dec 28	08:19:49	08:34:19	–77 (0.2)	11 (0.1)	–80 (–0.2)
J34	2021 Jun 7	16:53:40	16:59:00	22 (0.9)	12 (–0.1)	–76 (–0.5)

Notes. Jupiter magnetic fields are given in Ganymede-centric IAU coordinates in nT. The ranges for the Galileo flybys G1–G29 identify the times used by Kivelson et al. (2002), and J34 identifies the times used by Weber et al. (2022) to fit the magnetic moments; we use the same times in our calculations for Ganymede's internal magnetic field. Linearly interpolated Jupiter background fields B_x^J, B_y^J, and B_z^J are given as mean within the indicated times ("mn") in nT and slope ("slp") in nT minute^{-1}.

component of Jupiter's magnetic field B_x^J, B_y^J, and B_z^J as a linear function of time for each flyby. The slopes of the linear approximation depend on the spacecraft velocity as well as temporal changes in the external field. This linear representation is a fair approximation over the roughly 0.3 hr each spacecraft spends within Ganymede's magnetosphere on each flyby, as this timescale is much shorter than the main periods of oscillation from Jupiter's field: the synodic period relative to Jupiter's rotation (10.5 hr) and Ganymede's orbital period (171.7 hr). After accounting for the differences in coordinate systems used, we obtain approximately equivalent values for the mean of $\boldsymbol{B}^J$ as those of Kivelson et al. (2002) for most flybys (cf. Table 1 with Table 1 of Kivelson et al. 2002). We estimate transition times into and out of Ganymede's magnetosphere based on observed changes of the magnetic field direction in the data (Figure 2). The ranges of time over which we include measurements for our analysis (Table 1) are well within our estimations of the extent of Ganymede's magnetosphere (Figure 2) and are chosen to minimize contamination from the dynamic interactions between the Jovian plasma and Ganymede's magnetosphere (Paty & Winglee 2004; Jia et al. 2009; Collinson et al. 2018). Such contaminations are visible in the data as high-frequency fluctuations (Figure 2). The range for the Juno flyby is shorter than the ranges for the Galileo flybys because Juno traveled through Ganymede's magnetosphere at a higher velocity.

Following the approach of Kivelson et al. (2002), we model external fields $\boldsymbol{B}^U$ (containing, e.g., magnetopause fields) within Ganymede's magnetosphere as constant and uniform for each flyby. We note that, per flyby, we have two different external fields: Jupiter's field $\boldsymbol{B}^J$, which we subtract from the data before analysis, and the external field $\boldsymbol{B}^U$, which we calculate together with the spherical harmonic coefficients. Alternatively, a combined external field $\boldsymbol{B}^U+\boldsymbol{B}^J$ could be calculated along with the spherical harmonic coefficients instead of removing $\boldsymbol{B}^J$ first; we use the latter procedure for the most direct comparison of our work with prior studies. We calculate the spherical harmonic coefficients g_l^m and h_l^m for $\boldsymbol{B}^{\rm int}$ and the constant values for $\boldsymbol{B}^U$ from the data (Figure 2) by first subtracting Jupiter's field $\boldsymbol{B}^J$ (Table 1) from each flyby, then simultaneously solving for the internal spherical harmonic coefficients g_l^m and h_l^m as well as for each flyby's uniform (external) field values B_x^U, B_y^U, and B_z^U using a least-squares approach. Unlike Kivelson et al. (2002), we did not weight each flyby individually in our least-squares calculations.

2.2. Induced Fields

Oscillations in Jupiter's magnetic field as observed in Ganymede's reference frame give rise to induced magnetic moments inside Ganymede's conducting interior, primarily as an oscillating dipole moment (Styczinski et al. 2022). The intrinsic (core dynamo) magnetic moments of Ganymede are independent from the induced magnetic moments, but both are part of Ganymede's internal magnetic field $\boldsymbol{B}^{\rm int}$. As a consequence, contributions from induction $\boldsymbol{B}^{\rm ind}$ to the internal field $\boldsymbol{B}^{\rm int}$ could provide a source of systematic error in our analysis. To assess this error, we evaluate the induced magnetic field expected for plausible geophysical models of Ganymede's interior, including the hydrosphere. We subtract these induced fields from the spacecraft measurements along with the background field of Jupiter, prior to our least-squares fit for the intrinsic moments. The results of these analyses are then compared to the results from our analysis with the induction models omitted.

For the purpose of modeling the expected induced fields, we use the JRM33 model for Jupiter's intrinsic field (Connerney et al. 2022) along with the current sheet model of Connerney et al. (2020) to evaluate the strength of magnetic excitations as a function of frequency at Ganymede's location. For Ganymede's hydrospheric interior structure, we use the open-source PlanetProfile framework to generate depth-dependent electrical conductivity models for high- and low-salinity ocean cases (Vance et al. 2021), with ocean waters containing 10 wt% ("high" model) and 1 wt% ("low" model) $MgSO_4$, respectively, in addition to a model analogous to that of Saur et al. (2015), with a uniformly conducting ocean of conductivity 0.5 S m^{-1} ("simple" model). For these three models, the ice shell thicknesses are approximately 25 km, 94 km, and 120 km, respectively. Whereas the simple model has uniform conductivity in the ocean, the other models use depth-dependent conductivities, evaluated as a function of temperature and pressure based on a fit to laboratory measurements of $MgSO_4$ solutions (Vance et al. 2018). The induced field of Ganymede is evaluated as a function of time at the spacecraft locations using the input excitation moments and conductivity structure with the open-source MoonMag package (Styczinski 2022a). For simplicity, we assume Ganymede's ocean to be spherically symmetric with respect to Ganymede's IAU reference frame, and neglect induction from layers deeper than the ocean, which are likely to be well screened by the ocean.

We incorporate these induced field models by subtracting their values at the data locations and times from the Galileo and

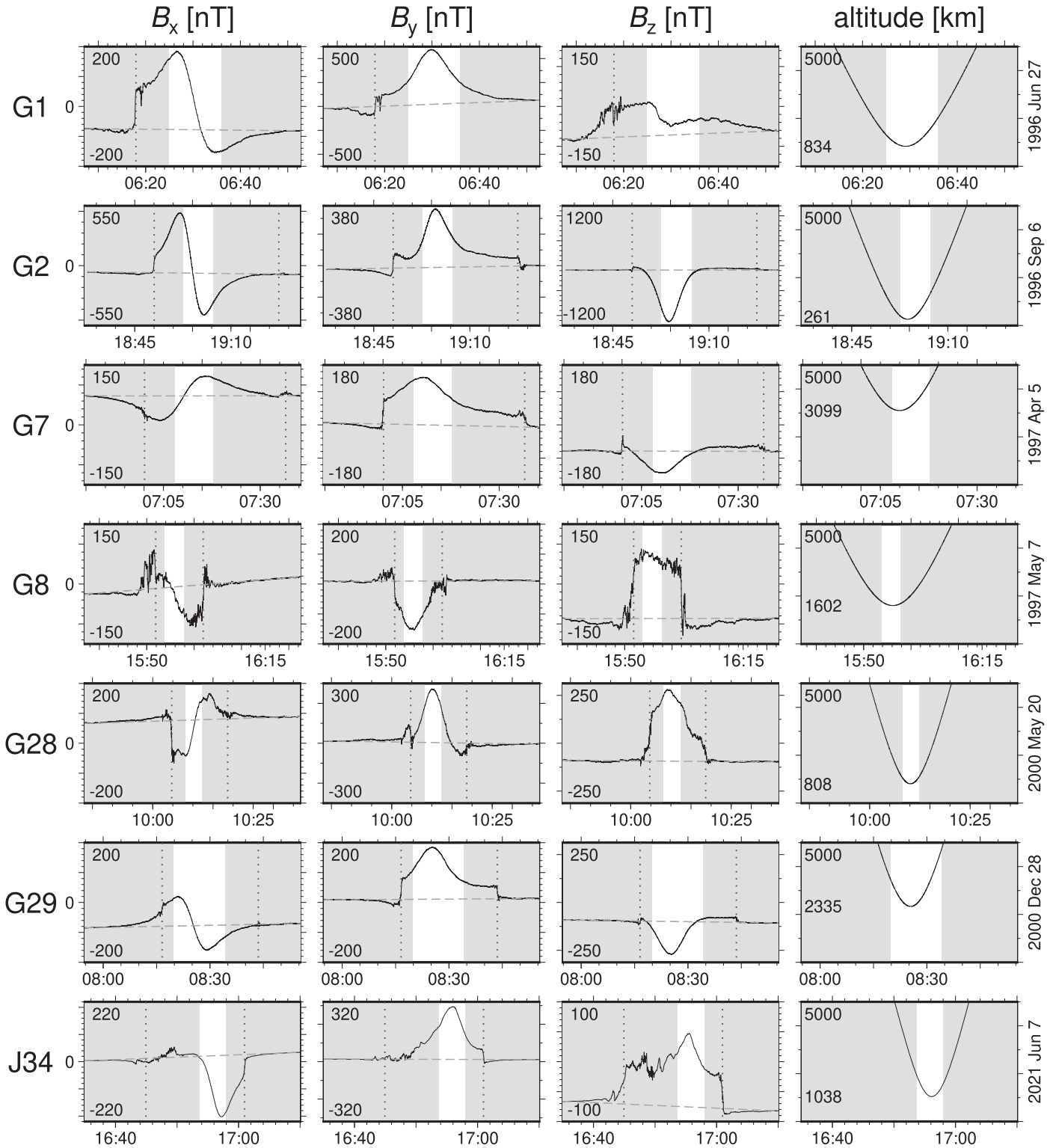

Figure 2. Raw data of the flybys of Galileo and Juno, including data before and after the encounter with Ganymede's magnetosphere in IAU coordinates. Dashed lines show Jupiter's background field (Table 1). Dotted vertical lines show estimated transitions into and out of Ganymede's magnetosphere, based on visually determined abrupt changes in the magnetic field measurements. The data time ranges used in our calculations for Ganymede's internal field are indicated by white bands and were taken from Kivelson et al. (2002) and Weber et al. (2022). Each panel has its own y-axis range, in nT for the magnetic data and km for the altitude data. Ranges are indicated in the top-left and bottom-left of each panel. Altitudes are above Ganymede's mean radius of $r_G = 2631.2$ km; the bottom of each altitude panel is 0, and the closest approach altitude of each flyby is labeled.

Juno data before solving for the intrinsic field models. In addition to these three hydrospheric structure models, "high," "low," and "simple," we also consider the case with ocean induction magnetic field ("–" model).

3. Results

For each ocean induction model ("–," "high," "low," and "simple"; see Section 2.2), we calculate spherical harmonic

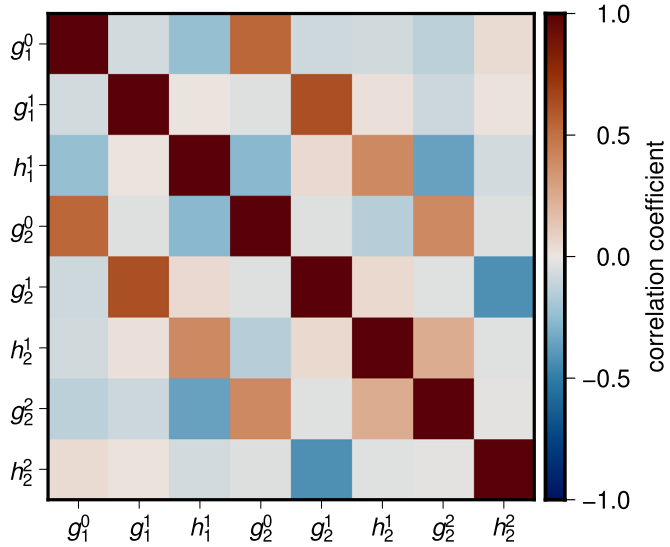

Figure 3. Correlation matrix for the spherical harmonic coefficients up to $L_{\max} = 2$ for the available flyby data (Figure 2, Table 1). For well-resolved coefficients, all cells off the diagonal must be close to zero (white). Red and blue cells off the diagonal indicate strong correlations and anticorrelations that prevent resolution of the intrinsic moments for Ganymede from existing flyby data.

models for two different maximum spherical harmonic degrees, $L_{\max} = 1$ and $L_{\max} = 2$, for Ganymede's internal magnetic field $\boldsymbol{B}^{\text{int}}$ using a least-squares approach without regularization. To assess how well the available data constrain the spherical harmonic coefficients, we conduct a correlation analysis (see the Appendix) of the linear system of equations that determines the spherical harmonic coefficients from the data locations (Figure 1). The corresponding correlation matrix (Figure 3) shows substantial correlations among coefficients. These correlations allow the signal to be fit equally well by a range of linear combinations of these coefficients.

Motivated by these strong correlations, we additionally assess two models, each with a fixed chosen spherical harmonic coefficient, to explore the space of models allowable by the data. We also use singular value decomposition (SVD), similar to Connerney (1981) and Burton et al. (2009, 2010), and remove a singular value and its corresponding columns of the orthogonal matrices in a generalized inversion calculation:

1. Dipole-only model ($L_{\max} = 1$): "L1."
2. Dipole + quadrupole ($L_{\max} = 2$): "L2A."
3. Dipole + quadrupole ($L_{\max} = 2$) with $h_2^1 = -47$ nT: "L2B."
4. Dipole + quadrupole ($L_{\max} = 2$) with $g_2^2 = 30$ nT: "L2C."
5. Dipole + quadrupole ($L_{\max} = 2$) with singular value number 24 removed: "L2D."
6. Dipole + quadrupole ($L_{\max} = 2$) with singular value number 25 removed: "L2E."

For models L2B and L2C, we choose the fixed values for the spherical harmonic coefficients h_2^1 and g_2^2, respectively, and solve for the remaining coefficients using a least-squares approach without regularization. The specific values for h_2^1 and g_2^2 are based on trial-and-error searches to minimize each model's data misfit and maximize its quadrupole power. For model L2D, we select for removal the singular value for which after removal the generalized inversion calculation yields the lowest data misfit compared to other choices of singular values. For model L2E, we select for removal a singular value leading to a higher quadrupolar strength. For each of L1, L2A, L2B, L2C, L2D, and L2E, we calculate a spherical harmonic model for each of the four ocean-induction models "–," "high," "low," and "simple," leading to a total of 24 models, which we name by appending the ocean model name to the spherical harmonic model name: "L1–," "L2Asimple," "L2Bhigh," etc.

To assess the uncertainty for each of our 24 models, we calculate 100 least-squares solutions, each for a 50% random subset of the data, and we report the mean spherical harmonic model and the standard deviation. All spherical harmonic models use the Galileo flybys G1, G2, G7, G8, G28, and G29, as well as Juno's flyby J34, collected on 2021 June 7 (Figure 2) for the time ranges indicated in Table 1.

The resulting uniform external fields $\boldsymbol{B}^U$ of our spherical harmonic models without including an ocean induction model ("–") agree with each other (Table 2). For the spherical harmonic coefficients g_l^m and h_l^m of these three models (Table 3), we observe quite different $l = 2$ coefficients, in particular for g_2^0, h_2^1, and g_2^2. This disagreement among coefficients derived for the same choice of $L_{\max}$ is substantially larger than the standard deviation of each of these coefficients.

For these models that neglect an ocean induction field, we observe small differences between their spatial patterns (Figure 4), in particular at the magnetic equator and in the southern hemisphere.

To assess whether any of the spherical harmonic models neglecting induction are favored based on the data available, we calculate the root mean square error (RMSE) of the data misfit from the difference between the calculated $\boldsymbol{B}^{\text{int}}+\boldsymbol{B}^U$ (Tables 2–3, Equations (2)–(3), using the mean coefficients) and the raw data after subtraction of $\boldsymbol{B}^J$ (Table 1). The overall RMSE of the least-squares models L2A–, L2B–, and L2C– are within 0.3 nT of each other (Table 4)—a small difference compared to the typical field magnitudes of ∼500 nT near closest approach. The SVD models L2D– and L2E– have higher RMSE (Table 4).

Comparisons between spacecraft data after subtracting $\boldsymbol{B}^J$ and modeled data $\boldsymbol{B}^{\text{int}}+\boldsymbol{B}^U$ (Figures 5 and 6) without incorporating ocean induction ("–") display long-wavelength differences in all components of all flybys shown. Kivelson et al. (2002) reported long-wavelength misfits in their GPhiO B_x components, which approximately correspond to the negative of our B_y components. The authors interpreted these misfits to result from external fields, specifically due to Alfvén wing bendback that was modeled neither in their approach nor ours. The models L2A– and L2B– show comparable structures in their misfits (Figure 6).

We observe that taking oceanic induction into account using the three proposed Ganymede internal structures "high," "low," and "simple" slightly increases the RMSE of the six models L1, L2A, L2B, L2C, L2D, and L2E (Table 5). In general, the induction model "high" leads to the strongest increase in RMSE, whereas the effects of "low" and "simple" are similar to each other.

4. Discussion

Previous spherical harmonic models of Ganymede's internal magnetic field were calculated from flybys G1, G2, G28 (Kivelson et al. 2002), and J34 (Weber et al. 2022). In this work, we use additional flybys. Repeating our calculations with

Table 2
Uniform Magnetic Field Components

Model	Comp	G1	G2	G7	G8	G28	G29	J34
L1–	$\boldsymbol{B}_x^U$	21 (0)	21 (0)	1 (0)	5 (0)	10 (0)	6 (0)	–3 (1)
	$\boldsymbol{B}_y^U$	33 (0)	77 (0)	43 (0)	54 (0)	–39 (1)	44 (0)	65 (1)
	$\boldsymbol{B}_z^U$	–15 (0)	23 (0)	12 (0)	90 (0)	73 (0)	10 (0)	–36 (0)
L2A–	$\boldsymbol{B}_x^U$	20 (0)	18 (0)	1 (0)	1 (0)	–1 (0)	6 (0)	–3 (0)
	$\boldsymbol{B}_y^U$	30 (0)	58 (0)	41 (0)	74 (1)	–52 (1)	41 (0)	61 (1)
	$\boldsymbol{B}_z^U$	–13 (0)	22 (0)	12 (0)	96 (0)	46 (1)	11 (0)	–37 (1)
L2B–	$\boldsymbol{B}_x^U$	21 (0)	16 (0)	1 (0)	0 (0)	–1 (0)	6 (0)	–2 (1)
	$\boldsymbol{B}_y^U$	35 (0)	47 (0)	41 (0)	83 (1)	–70 (1)	41 (0)	63 (1)
	$\boldsymbol{B}_z^U$	–7 (0)	15 (0)	12 (0)	95 (1)	38 (1)	10 (0)	–33 (0)
L2C–	$\boldsymbol{B}_x^U$	21 (0)	17 (0)	1 (0)	1 (0)	–1 (0)	6 (0)	–2 (1)
	$\boldsymbol{B}_y^U$	37 (0)	54 (1)	42 (0)	80 (1)	–50 (0)	43 (0)	67 (0)
	$\boldsymbol{B}_z^U$	–6 (0)	8 (0)	12 (0)	99 (0)	39 (1)	9 (0)	–34 (0)
L2D–	$\boldsymbol{B}_x^U$	16 (1)	20 (0)	1 (0)	–3 (0)	–8 (1)	6 (0)	5 (1)
	$\boldsymbol{B}_y^U$	19 (1)	84 (3)	42 (0)	68 (1)	–38 (2)	44 (0)	57 (1)
	$\boldsymbol{B}_z^U$	2 (2)	13 (1)	15 (0)	99 (1)	43 (1)	13 (0)	–34 (1)
L2E–	$\boldsymbol{B}_x^U$	13 (0)	27 (1)	0 (0)	12 (1)	10 (1)	6 (0)	2 (1)
	$\boldsymbol{B}_y^U$	30 (0)	75 (1)	42 (0)	78 (0)	–28 (2)	44 (0)	56 (1)
	$\boldsymbol{B}_z^U$	–8 (0)	10 (1)	13 (0)	104 (1)	30 (1)	11 (0)	–23 (1)

Notes. Values, in nT, rounded to the nearest integer represent the model averages. One standard deviation rounded to the nearest integer is indicated in parentheses.

Table 3
Spherical Harmonic Coefficients of Our Intrinsic Magnetic Field Models $\boldsymbol{B}^{\mathrm{int}}$

Model	g_1^0	g_1^1 h_1^1	g_2^0	g_2^1 h_2^1	g_2^2 h_2^2
L1–	–725.3 (0.2)	74.2 (0.3) 19.5 (0.4)	0 (0*)	0 (0*) 0 (0*)	0 (0*) 0 (0*)
L2A–	–761.4 (1.0)	58.9 (0.5) 12.0 (0.7)	21.4 (0.6)	4.5 (0.4) –20.8 (0.5)	6.8 (0.4) –16.5 (0.3)
L2B–	–766.9 (1.0)	61.2 (0.4) 23.5 (0.8)	21.8 (0.6)	–0.4 (0.3) –47.0 (0*)	18.1 (0.5) –21.3 (0.2)
L2C–	–752.8 (1.1)	64.4 (0.5) 16.4 (0.7)	16.8 (0.7)	–0.7 (0.4) –37.3 (0.3)	30.0 (0*) –21.7 (0.3)
L2D–	–760.0 (1.0)	59.5 (0.5) 20.5 (1.0)	37.9 (1.8)	4.8 (0.4) –3.3 (1.9)	19.5 (1.4) –31.8 (1.5)
L2E–	–758.5 (1.0)	62.2 (0.3) 10.8 (0.8)	30.1 (0.6)	27.8 (1.25) –18.0 (0.7)	41.6 (1.1) 25.1 (1.5)

Notes. Values, in nT, represent the model averages, with one standard deviation indicated in parentheses. The standard deviations marked with an asterisk * are zero because the corresponding coefficients are set to a fixed value.

only G1, G2, G28, and J34 (to compare with past studies) has a negligible effect on our results.

We found a range of intrinsic magnetic field models for Ganymede that fit the data similarly well and which use the same maximum spherical harmonic degree 2. This result indicates that for presently available data, there is a large uncertainty in the quadrupolar spherical harmonic coefficients. To assess whether selecting a model resolving the quadrupolar moment (L2A, L2B, L2C, L2D, L2E) over a purely dipolar model (L1) is justified, we carry out a leave-one-out cross-validation. For each model, we omit one of the flybys, obtain the least-squares solution from the remaining flybys, and then calculate the RMSE of the resulting model for the omitted flyby, using the $\boldsymbol{B}^U$ values of Table 2. Repeating this approach for each flyby yields seven RMSE per model (one RMSE for each flyby). We calculate the "leave-one-out cross-validation" for a model as the rms of these seven RMSE. If a model has a high leave-one-out cross-validation, then this model likely

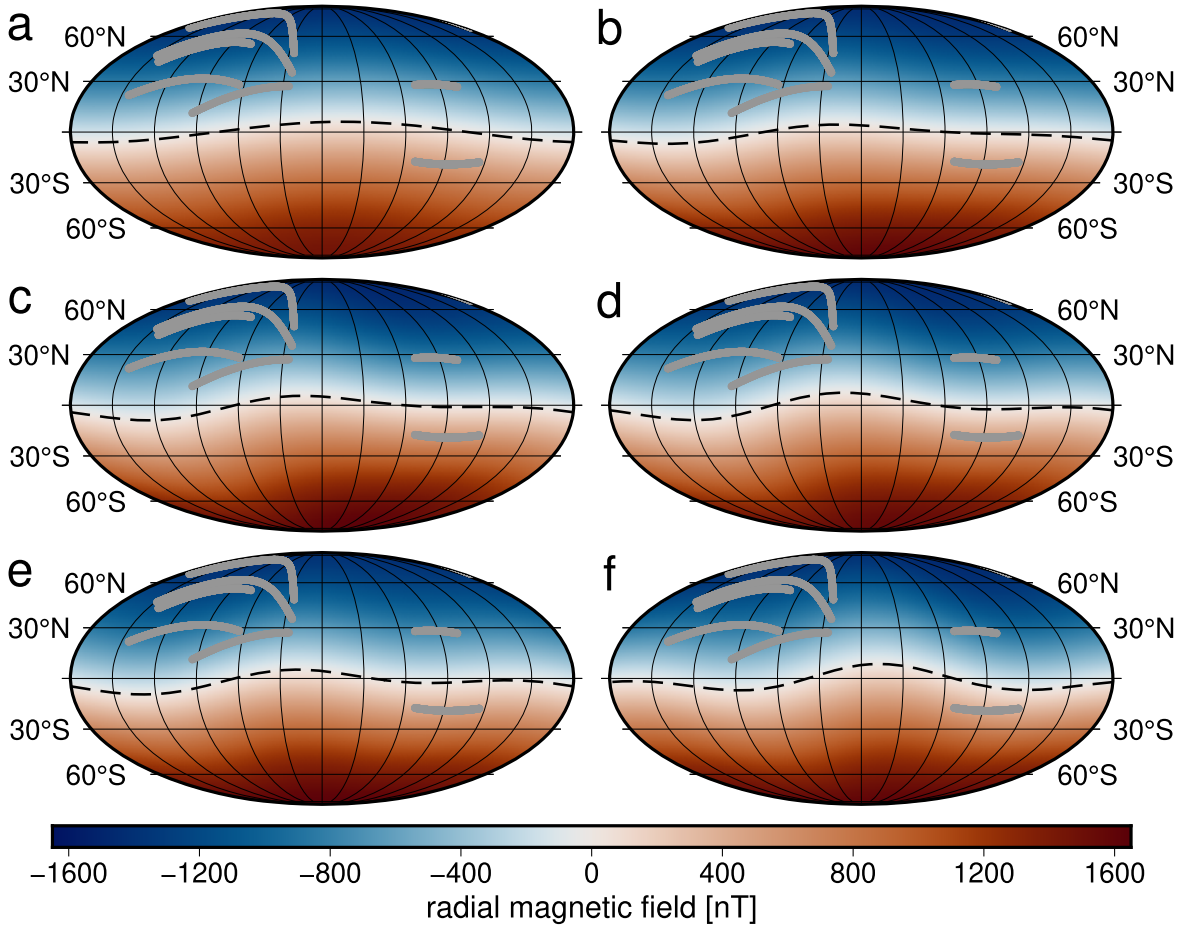

Figure 4. Radial component of the internal magnetic field models $\boldsymbol{B}^{\rm int}$ from Table 3 (no ocean induction) plotted on Ganymede's surface ($r_G = 2631.2$ km), together with the corresponding data locations that were used in the internal field calculations. Black dashed lines indicate magnetic equators. (a) L1–, (b) L2A–, (c) L2B–, (d) L2C–, (e) L2D–, (f) L2E–.

Table 4
RMSE for Mean Spherical Harmonic Models

Model	G1	G2	G28	J34	Total
L1–	6.0	4.3	12.4	8.2	7.0
L2A–	5.3	3.5	9.5	8.4	6.2
L2B–	5.4	4.4	10.7	7.4	6.5
L2C–	6.2	3.7	9.9	8.2	6.5
L2D–	10.6	9.0	9.8	8.1	7.8
L2E–	12.7	9.7	14.4	9.7	9.7

Notes. Values given in nT. RMSE are given for select flybys and in total, calculated as the rms of the RMSE of G1, G2, G7, G8, G28, G29, and J34.

overfits the available data compared to a model with a lower leave-one-out cross-validation. We find that model L1 has the lowest leave-one-out cross-validation (Table 6). Thus, models that use a quadrupole moment overfit the data. The leave-one-out cross-validation values for the quadrupolar models are similar, with the models for fixed coefficients (L2B, L2C) having lower values compared to the SVD-derived models (L2D, L2E).

A possible approach to reduce the spread of allowable quadrupolar moments could be to impose regularization (e.g., Bloxham et al. 1989; Parker 1994; Johnson & Constable 1995; Holme & Bloxham 1996a, 1996b; Uno et al. 2009). Regularization allows the construction of smooth, minimally structured models. Unfortunately, for sparse data coverage such regularization affects the power spectrum, even at the low spherical harmonic degrees that we study (e.g., Uno et al. 2009, their Figure 3(c)). One of the goals of our study is to assess the relative powers of the spherical harmonic degrees of Ganymede's intrinsic field. Thus, regularization would predetermine the very information we aim to extract.

The range of presented models for the intrinsic field (Section 3) limits what conclusions can be drawn from the presently available magnetic field data for Ganymede. For the intrinsic field of Kivelson et al. (2002), Christensen (2015a, 2015b) calculated a quadrupole-to-dipole ratio ($R(2)/R(1)$ for $R(l)$ in Equation (4)) of 0.04 for a presumed core–mantle boundary (CMB) radius of 658 km, corresponding to $0.25r_G$. Christensen concluded that this was an exceptionally low quadrupole-to-dipole ratio compared to most planets in our solar system, with the possible exception of Saturn. For our model L2A– we obtain a similar ratio for a CMB radius of $0.25r_G$ (Table 7). For our model L2B–, however, we obtain a substantially larger ratio of 0.14 (Table 7). This ratio is equal to Earth's core magnetic field quadrupole-to-dipole ratio at Earth's CMB (Christensen 2015a). Care must be taken when using quadrupole-to-dipole ratios to determine the radius of a core dynamo. The dipole and quadrupole strengths tend to not follow the trend observed in the powers $R(l)$ of spherical harmonic degrees $l \geqslant 3$ (Lowes 1974). Thus, calculating a dynamo radius from analytically derived power spectra (such

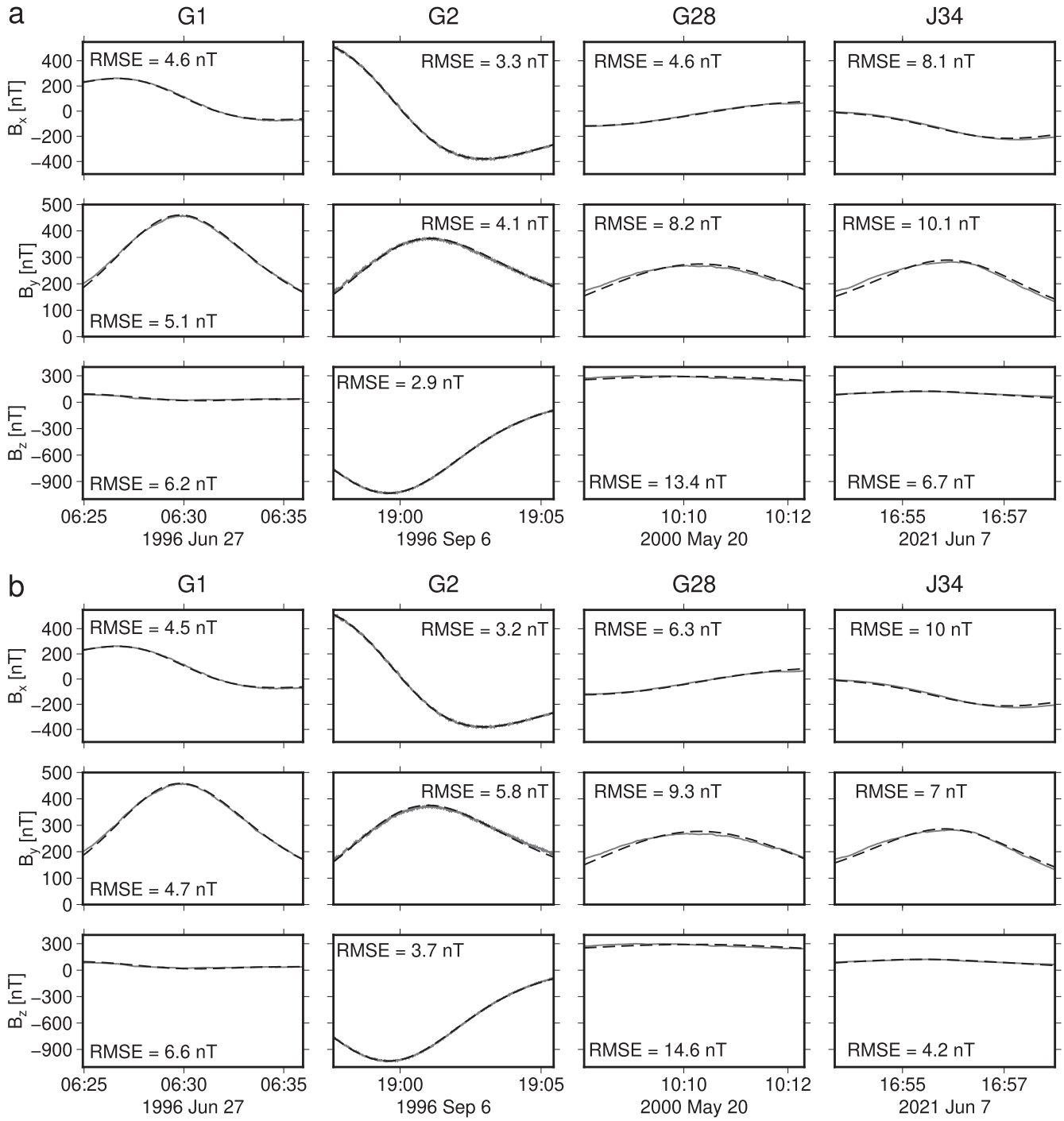

Figure 5. Data after subtraction of $\boldsymbol{B}^J$ (gray solid lines) and modeled data $\boldsymbol{B}^{\text{int}}+\boldsymbol{B}^U$ (black dashed lines) from models (a) L2A– and (b) L2B–, shown for flybys G1, G2, G28, and J34.

as, e.g., Voorhies et al. 2002) using the quadrupole-to-dipole ratio yields spurious results. To avoid this issue, Christensen (2015a, 2015b) instead calculated quadrupole-to-dipole ratios from the outcomes of magnetohydrodynamic simulations. Christensen determined which parameters used in his simulations yielded comparable values to the results of Kivelson et al. (2002). Our inferred uncertainty of the spherical harmonic coefficients for Ganymede's intrinsic field thus allows for more of the dynamo models of Christensen (2015a, 2015b), and not only for a subset with low quadrupole-to-dipole ratio. This analysis broadens the range of explanations for Ganymede's dynamo. Our intrinsic field models taking ocean induction into account produced slightly lower quadrupole-to-dipole ratios compared to models without ocean induction. This indicates that ocean induction may contribute to the observed quadrupolar power, but even with a high-salinity ocean Ganymede's quadrupole-to-dipole ratio remains poorly constrained (Table 7).

We use a least-squares approach to solve for spherical harmonic coefficients from the available data as well as a SVD generalized inversion. Other methods may yield different coefficients. We note that the existence of our solutions

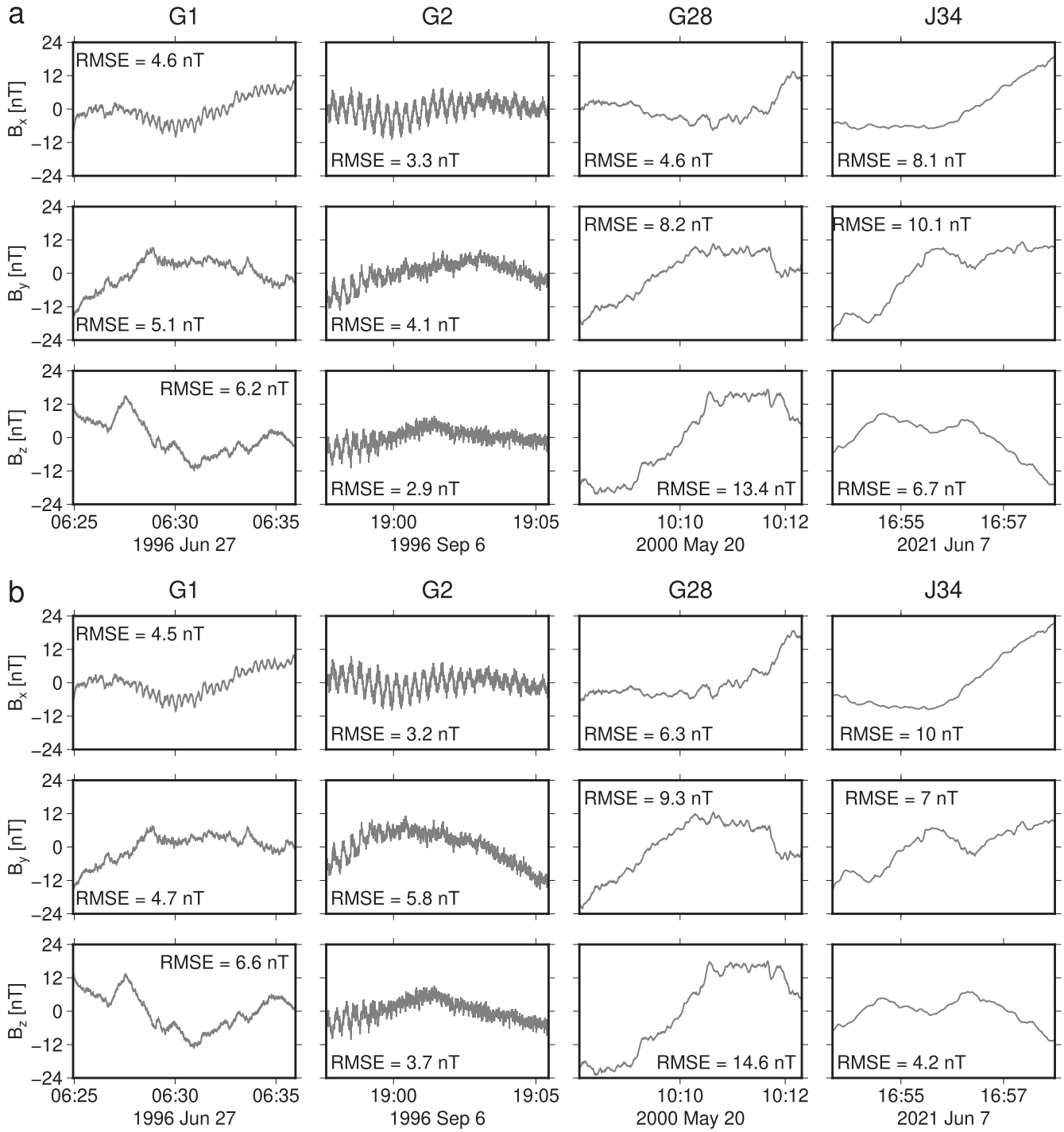

Figure 6. Differences between the spacecraft data and the modeled data in Figure 5 for (a) L2A– and (b) L2B–, shown for flybys G1, G2, G28, and J34.

together with their data misfits, and the correlation analysis that is governed by the spatial distribution of the data, provide evidence for a range of possible spherical harmonic models, no matter how these models were obtained. Thus, using more sophisticated approaches to solve for global spherical harmonic models would not resolve this uncertainty given the available data. We acknowledge that our approach likely underestimates the nonuniqueness of solving for quadrupolar components from the presently available data, and we do not claim that our study characterizes the full solution space. We demonstrate that there exists at least one solution with a quadrupole-to-dipole ratio similar to that of Earth and which fits the data equally well (within 0.2 nT) compared to a solution with a substantially smaller quadrupole-to-dipole ratio.

We emphasize that our goal is to study the uncertainty of intrinsic spherical harmonic magnetic field models and the effect of these uncertainties on interpreting dynamo models. Because the expressions relating the data to the spherical harmonic coefficients (Equations (2) and (3)) are linear, linear combinations of the resulting spherical harmonic coefficients for models with identically modeled ocean induction also solve these equations, so long as the weights of the models in a linear combination sum to unity. From linear combinations of our models L2A– and L2B–, we construct models for which the

Table 5
Total RMSE of Spherical Harmonic Models

Model	Ocean Induction Model			
	–	High	Low	Simple
L1	7.0	9.1	8.6	8.6
L2A	6.2	8.9	8.4	8.4
L2B	6.5	9.0	8.6	8.6
L2C	6.5	9.0	8.5	8.5
L2D	7.8	10.1	9.7	9.7
L2E	9.7	11.5	11.2	11.2

Notes. Values in nT. The symbol "–" indicates no ocean induction; "high" and "low" are with a high- and low-salinity ocean, respectively; "simple" is for an ocean with a uniform conductivity (see Section 2.2).

Table 6
Leave-one-out Cross-validation

Model	Ocean Induction Model			
	–	High	Low	Simple
L1	7.8	6.9	6.9	6.9
L2A	17.1	15.2	15.3	15.2
L2B	16.7	15.6	15.7	15.7
L2C	14.9	15.5	15.5	15.5
L2D	20.2	19.7	19.5	19.4
L2E	21.8	19.8	19.8	19.8

Notes. Values in nT, obtained by skipping individual flybys (see text). The symbol "–" indicates that no ocean induction model was used; "high," "low," and "simple" indicate the ocean induction models described in Section 2.2.

Table 7
Quadrupole-to-dipole Ratios

Model	r_G	$0.3r_G$	$0.25r_G$
L2A–	0.003	0.04	0.05
L2B–	0.009	0.10	0.14
L2C–	0.008	0.09	0.13
L2D–	0.008	0.08	0.12
L2E–	0.010	0.13	0.19
L2A+	0.002	0.02	0.04
L2B+	0.007	0.09	0.13
L2C+	0.006	0.07	0.10
L2D+	0.006	0.06	0.09
L2E+	0.010	0.12	0.17

Notes. The symbol "+" indicates with and the symbol "–" without taking into account ocean induction. The quadrupole-to-dipole ratios rounded to significant digits were the same for the three different ocean induction models, "high," "low," and "simple," thus we represent them all with the model abbreviations L2A+, L2B+, L2C+, L2D+, and L2E+.

quadrupole-to-dipole ratio at $0.25r_G$ cover the full range from extremely low, to Jupiter-like (0.1; Christensen 2015a), to Earth-like (0.14; Christensen 2015a; see Figure 7). The RMSE values of these models are within 0.3 nT of each other—a small difference considering typical field magnitudes of ∼500 nT.

The physical fidelity of our models is limited by the use of uniform fields to represent the external field contributions $\boldsymbol{B}^U$ from plasma interactions with Ganymede's magnetosphere. Uniform external fields are an external field representation of

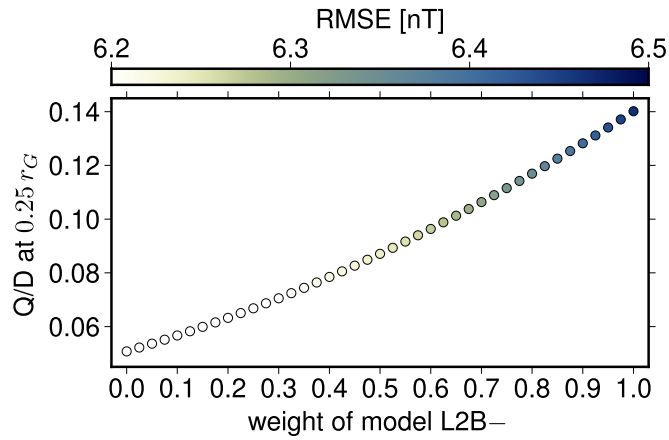

Figure 7. Quadrupole-to-dipole ratio (Q/D) at $0.25r_G$ for linear combinations of models L2A– and L2B–, with weights summing to unity.

spherical harmonic degree 1. Plasma interactions will contribute short-period fluctuations in the measured magnetic field, essentially contributing systematic noise in the data. A spatially varying potential field can be used to more accurately describe the external field, but we do not expect that such a representation would alter our conclusions as it would add more variables to resolve and thus further reduce the uniqueness of the solution, which we have already shown to be too weak to draw conclusions about the power of the quadrupole component.

The spatial differences between our models L2A–, L2B–, and L2C– show that the area of greatest disagreement is in the southern hemisphere, in particular the southern part of the leading hemisphere (Figure 8). Additional flybys covering that area may reduce the correlations among spherical harmonic coefficients (Figure 3) and ultimately provide better constraints on Ganymede's core magnetic field.

We examine the effect of induced fields from Ganymede's putative ocean on our results by forward modeling plausible interior structures and subtracting the induced field expected from each model from the flyby measurements. Taking ocean induction into account reduces the leave-one-out cross-validation of our models (Table 6). We interpret this as an indication that ocean induction is present in the magnetic field data. However, available data cannot distinguish between our three end-member ocean models "high," "low," and "simple" (see Section 2.2). Solving for a dipole as well as a quadrupole moment, our models L2B and L2C with any of the three ocean induction models yields a similar RMSE as the corresponding ocean induction for model L2A (Table 5). These results contrast with the interpretation of Saur et al. (2015) that induced fields on Ganymede meant that the quadrupole strengths of Kivelson et al. (2002) were an upper bound. Instead, we find that presently available data simply cannot constrain Ganymede's intrinsic quadrupolar moment.

5. Conclusions

Our results demonstrate that presently available data cannot sufficiently constrain the quadrupole power of Ganymede's core magnetic field globally. Our range of spherical harmonic models indicates that a variety of dynamo models may be plausible for Ganymede. We argue that a dynamo operating in a substantial part of Ganymede's core is plausible and may present a simpler solution than a dynamo operating only within

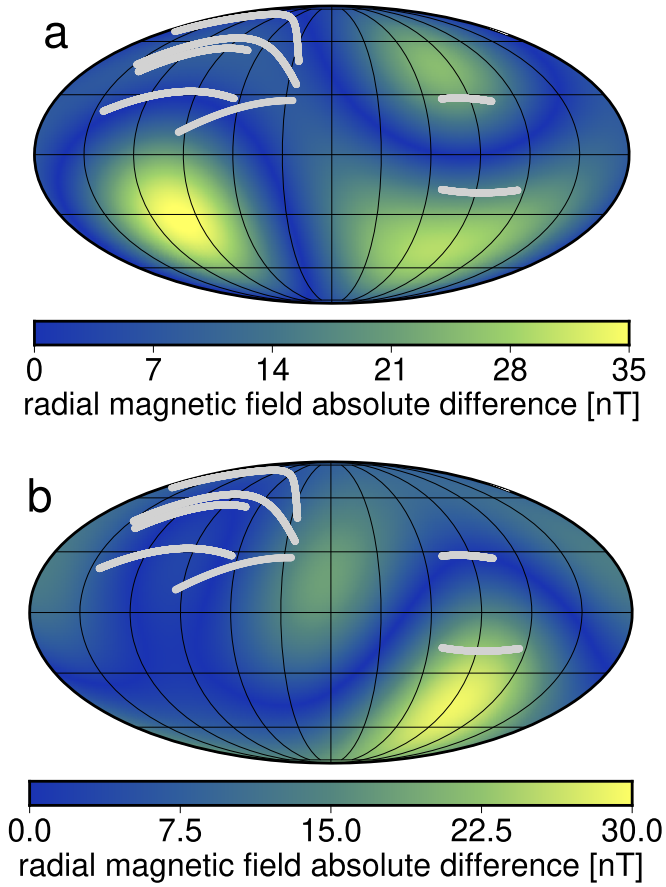

Figure 8. Absolute difference of the radial components between (a) models L2A– and L2B–, and (c) models L2B– and L2C–. Flyby ground tracks, denoted by gray lines, are mostly clustered in specific northern regions. The projection is the same as in Figure 1.

a small fraction of Ganymede's core. Presently available data cannot distinguish between these possibilities. Available data allow for ocean induction but cannot discern a best fit from among the range of ocean induction models we tested. Once JUICE orbital data of Ganymede become available (Grasset et al. 2013), we expect that Ganymede's core magnetic field will be robustly determined to higher spherical harmonic degrees, and assessment of ocean induction will become possible, providing scientific closure on these research questions.

Acknowledgments

This work was supported by NASA under grant No. 80NSSC20K1080. M.J.S. was supported by an appointment to the NASA Postdoctoral Program at the Jet Propulsion Laboratory, California Institute of Technology, administered by Oak Ridge Associated Universities under a contract with NASA (grant No. 80HQTR21CA005). Part of this work was supported by the Icy Worlds node of the NASA Astrobiology Institute, (13-NAI7-0024) and was carried out at the Jet Propulsion Laboratory, California Institute of Technology, under a contract with NASA (grant No. 80NM0018D0004). C. L.J. acknowledges support from the Discovery Grants program of the Natural Sciences and Engineering Research Council of Canada. All figures were made using GMT (Wessel et al. 2013, 2019).

Spacecraft data were obtained from the Planetary Data System (PDS) Planetary Plasma Interactions (PPI) Node: volumes GO-J-POS-6-SC-TRAJ-MOON-COORDS-V1.0 (Galileo position), GO-J-MAG-3-RDR-HIGHRES-V1.0 (Galileo magnetic field data), and JNO-J-3-FGM-CAL-V1.0 (Juno magnetic field data). We use the software package "SpiceyPy" (Annex et al. 2020) to transform Juno data from Jupiter planetocentric coordinates to Ganymede IAU coordinates. Software to reproduce this research is available on NASA's Planetary Science GitHub page (https://github.com/NASA-Planetary-Science/GanymedeMagModels) and archived at doi:10.5281/zenodo.6728370. Some data used in this work were generated using the open-source PlanetProfile (v1.1.0; Vance et al. 2020) and MoonMag (v1.2.3; Styczinski 2022b) frameworks.

Appendix
Correlation Analysis

To obtain the spherical harmonic coefficients g_l^m and h_l^m from the three components of the magnetic field data $\boldsymbol{B}_x$, $\boldsymbol{B}_y$, and $\boldsymbol{B}_z$, we combine Equations (2) and (3) and use the measurements of $\boldsymbol{B}^{\text{int}}$ as the known right-hand side $\boldsymbol{b}$. In this linear system of equations, the evaluated spherical harmonics at the data locations r, θ, and ϕ constitute the matrix $\mathbf{A}$, and the coefficients g_l^m and h_l^m are the unknowns $\boldsymbol{u}$ in

$$\mathbf{A}\boldsymbol{u} = \boldsymbol{b}. \tag{A1}$$

Because the number of data locations is greater than the number of unknowns, this system of equations is solved in a least-squares sense. Although this system of equations is overdetermined, the constraints on the coefficients (unknowns) may not be uncorrelated. To test the correlation between the unknowns, we conduct a correlation analysis of the columns $\boldsymbol{A}_i$ of the matrix $\mathbf{A}$c. We consider the entries of each column as evaluations of a random variable and measure the correlations between the columns as

$$\rho_{i,j} = \frac{1}{N-1}\sum_{k=1}^{N}\left(\frac{A_{i,k}-\mu_i}{\sigma_i}\right)\left(\frac{A_{j,k}-\mu_j}{\sigma_j}\right), \tag{A2}$$

where N is the number of data locations multiplied by 3, because we have three vector components per data location, μ_i is the mean of the ith column of matrix $\mathbf{A}$, and σ_i is the standard deviation of the ith column of matrix $\mathbf{A}$. The resulting correlation values $\rho_{i,j}$ are a measure of how strongly the unknowns $\boldsymbol{u}_i$ and $\boldsymbol{u}_j$ are correlated based on the given data locations, i.e., how much the solution for one unknown is affected by the solution for the other. Under ideal data distributions, the unknowns are uncorrelated, because the analytical multipole moments are mutually orthogonal.

Figure 3 shows the correlation values $\rho_{i,j}$ for the spherical harmonic coefficients based on the data locations. The substantial correlations observed indicate that different solutions can fit the data values similarly well. Note that we did not take the uniform fields $\boldsymbol{B}^U$ into account in our correlation analysis.

ORCID iDs

A. M. Plattner https://orcid.org/0000-0001-5154-1833
M. J. Styczinski https://orcid.org/0000-0003-4048-5914
S. D. Vance https://orcid.org/0000-0002-4242-3293

References

Annex, A. M., Pearson, B., Seignovert, B., et al. 2020, JOSS, 5, 2050
Blakely, R. J. 1995, Potential Theory in Gravity Magnetic Applications (Cambridge: Cambridge Univ. Press)
Bland, M. T., Showman, A. P., & Tobie, G. 2008, Icar, 198, 384
Bloxham, J., Gubbins, D., & Jackson, A. 1989, RSPTA, 329, 415
Burton, M., Dougherty, M., & Russell, C. 2009, P&SS, 57, 1706
Burton, M. E., Dougherty, M. K., & Russell, C. T. 2010, GeoRL, 37, L24105
Christensen, U. R. 2015a, Icar, 247, 248
Christensen, U. R. 2015b, Icar, 256, 63
Collinson, G., Paterson, W. R., Bard, C., et al. 2018, GeoRL, 45, 3382
Connerney, J. E. P. 1981, JGR, 86, 7679
Connerney, J. E. P., Timmins, S., Herceg, M., & Joergensen, J. L. 2020, JGRA, 125, e2020JA028138
Connerney, J. E. P., Timmins, S., Oliversen, R. J., et al. 2022, JGRE, 127, e2021JE007055
Grasset, O., Dougherty, M. K., Coustenis, A., et al. 2013, P&SS, 78, 1
Hauck, S. A., II, Aurnou, J. M., & Dombard, A. J. 2006, JGR, 111, E09008
Holme, R., & Bloxham, J. 1996a, JGR, 101, 2177
Holme, R., & Bloxham, J. 1996b, PEPI, 98, 221
Jia, X., Walker, R. J., Kivelson, M. G., Khurana, K. K., & Linker, J. A. 2009, JGRA, 114, A09209
Johnson, C., & Constable, C. 1995, GeoJI, 122, 489
Kivelson, M. G., Khurana, K. K., Russell, C. T., et al. 1996, Natur, 384, 537
Kivelson, M. G., Khurana, K. K., & Volwerk, M. 2002, Icar, 157, 507
Lowes, F. J. 1974, GeoJI, 36, 717
Parker, R. L. 1994, Geophysical Inverse Theory (Princeton, NJ: Princeton Univ. Press)
Paty, C., & Winglee, R. 2004, GeoRL, 31, L24806
Rückriemen, T., Breuer, D., & Spohn, T. 2015, JGRE, 120, 1095
Sarson, G. R., Jones, C. A., Zhang, K., & Schubert, G. 1997, Sci, 276, 1106
Saur, J., Duling, S., Roth, L., et al. 2015, JGRA, 120, 1715
Schubert, G., Anderson, J. D., Spohn, T., & McKinnon, W. B. 2004, in Jupiter. The Planet, Satellites and Magnetosphere, ed. F. Bagenal, T. E. Dowling, & W. B. McKinnon (Cambridge: Cambridge Univ. Press), 281
Schubert, G., Zhang, K., Kivelson, M. G., & Anderson, J. D. 1996, Natur, 348, 544
Styczinski, M. J. 2022a, MoonMag, v1.5.2, Zenodo, doi:10.5281/zenodo.7363749
Styczinski, M. 2022b, MoonMag: Repackaged for distribution with PyPI, v1.2.3, Zenodo, doi:10.5281/zenodo.6460643
Styczinski, M. J., Vance, S. D., Harnett, E. M., & Cochrane, C. J. 2022, Icar, 376, 114840
Uno, H., Johnson, C. L., Anderson, B. J., Korth, H., & Solomon, S. C. 2009, E&PSL, 285, 328
Vance, S. D., Panning, M. P., Stähler, S., et al. 2018, JGRE, 123, 180
Vance, S. D., Styczinski, M. J., Bills, B. G., et al. 2021, JGRE, 126, e2020JE006418
Vance, S., Styczinski, M., Melwani Daswani, M., & Vega, K. 2020, PlanetProfile: Supplementary Data: Magnetic Induction Responses of Jupiter's Ocean Moons Including Effects from Adiabatic Convection, v1.1.0, Zenodo, doi:10.5281/zenodo.4052711
Voorhies, C. V., Sabaka, T. J., & Purucker, M. 2002, JGRE, 107, 5034
Weber, T., Moore, K., Connerney, J., et al. 2022, GeoRL, 49, e2022GL098633
Wessel, P., Luis, J. F., Uieda, L., et al. 2019, GGG, 20, 5556
Wessel, P., Smith, W. H. F., Scharroo, R., Luis, J. F., & Wobbe, F. 2013, EOSTr, 94, 409
Winch, D. E., Ivers, D. J., Turner, J. P. R., & Stening, R. J. 2005, GeoJI, 160, 487
Zhan, X., & Schubert, G. 2012, JGRE, 117, E08011